

IC 348-SMM2E: a Class 0 proto-brown dwarf candidate forming as a scaled-down version of low-mass stars

Aina Palau^{1*}, Luis A. Zapata¹, Luis F. Rodríguez¹, Hervé Bouy², David Barrado², María Morales-Calderón², Philip C. Myers³, Nicholas Chapman⁴, Carmen Juárez⁵, Di Li^{6,7}

¹ Centro de Radioastronomía y Astrofísica, Universidad Nacional Autónoma de México, P.O. Box 3-72, 58090 Morelia, Michoacán, México

² Centro de Astrobiología, INTA-CSIC, Depto. Astrofísica, ESAC Campus, P.O. Box 78, 28691 Villanueva de la Cañada, Madrid, Spain

³ Harvard-Smithsonian Center for Astrophysics, 60 Garden Street, Cambridge, MA 02138, USA

⁴ Center for Interdisciplinary Exploration and Research in Astrophysics (CIERA) and Department of Physics & Astronomy, Northwestern University, 2145 Sheridan Road, Evanston, IL 60208, USA

⁵ Institut de Ciències de l'Espai (CSIC-IEEC), Campus UAB-Facultat de Ciències, Torre C5-parell 2, 08193 Bellaterra, Catalunya, Spain

⁶ National Astronomical Observatories, Chinese Academy of Sciences, Beijing 100012, China

⁷ Space Science Institute, Boulder, CO. 80301, USA

Accepted date. Received date; in original form date

ABSTRACT

We report on Submillimeter Array observations of the 870 μm continuum and CO (3–2), ^{13}CO (2–1) and C^{18}O (2–1) line emission of a faint object, SMM2E, near the driving source of the HH 797 outflow in the IC 348 cluster. The continuum emission shows an unresolved source for which we estimate a mass of gas and dust of $30 M_{\text{Jup}}$, and the CO (3–2) line reveals a compact bipolar outflow centred on SMM2E, and barely seen also in ^{13}CO (2–1). In addition, C^{18}O (2–1) emission reveals hints of a possible rotating envelope/disk perpendicular to the outflow, for which we infer a dynamical mass of $\sim 16 M_{\text{Jup}}$. In order to further constrain the accreted mass of the object, we gathered data from *Spitzer*, *Herschel*, and new and archive submillimetre observations, and built the Spectral Energy Distribution (SED). The SED can be fitted with one single modified black-body from 70 μm down to 2.1 cm, using a dust temperature of ~ 24 K, a dust emissivity index of 0.8, and an envelope mass of $\sim 35 M_{\text{Jup}}$. The bolometric luminosity is $0.10 L_{\odot}$, and the bolometric temperature is 35 K. Thus, SMM2E is comparable to the known Class 0 objects in the stellar domain. An estimate of the final mass indicates that SMM2E will most likely remain substellar, and the SMM2E outflow force matches the trend with luminosity known for young stellar objects. Thus, SMM2E constitutes an excellent example of a Class 0 proto-brown dwarf candidate which forms as a scaled-down version of low-mass stars. Finally, SMM2E seems to be part of a wide (~ 2400 AU) multiple system of Class 0 sources.

Key words: stars: formation — stars: brown dwarfs — ISM: individual objects: IC348-SMM2, HH 797 — ISM: lines and bands — ISM: jets and outflows — submillimetre: ISM

1 INTRODUCTION

The formation of brown-dwarfs (BDs) remains a highly debated field of current astrophysics. BD masses ($< 0.075 M_{\odot}$) are much smaller than Jeans masses estimated for typical conditions of molecular clouds ($\sim 1 M_{\odot}$), and their formation cannot be simply explained as a scaled-down version of low-mass stars. Several mechanisms have been proposed to

solve this problem, such as ejection from fragmented massive disks (e. g., Rice et al. 2003; Stamatellos & Whitworth 2009; Basu & Vorobyov 2012) or from multiple systems (Reipurth & Clarke 2001; Bate, Bonnell & Broom 2002; Umbreit et al. 2005), photo-erosion by nearby massive stars (e. g., Hester et al. 1996; Whitworth & Zinnecker 2004), and the formation of cores of very low Jeans masses through gravoturbulent fragmentation (e. g., Padoan & Nordlund 2004; Hennebelle & Chabrier 2008; Chabrier et al. 2014). A method to distinguish which of these mechanisms dominates is to study

* E-mail: a.palau@crya.unam.mx

BDs in their most embedded stages of their formation, comparable to the Class 0/I stages of low-mass star formation (e.g., André, Ward-Thompson, & Barsony 1993), called here ‘proto-BDs’. If BDs form as low-mass stars, one would expect substantial envelopes and outflows as observed in young stellar objects.

With the great sensitivity of the *Spitzer Space Telescope*, a new family of objects emerged, the so-called Very Low Luminosity Objects (VeLLOs), which are young stellar objects in a quiescent accretion phase, or potential proto-BD candidates and very low-mass stars. VeLLOs are most of them associated with infrared sources and present internal luminosities $\lesssim 0.1 L_{\odot}$ (e.g., Young et al. 2004; di Francesco et al. 2007; Dunham et al. 2008; Hsieh & Lai 2013). However, recent attempts to search for molecular outflows have reported a striking low detection rate (Schwarz et al. 2012), probably because their low-velocity wings cannot be separated from the large-scale ambient cloud emission detected by single-dish telescopes. Thus, most of the VeLLOs need to be studied with millimetre interferometry, making difficult to infer general properties in a statistically significant sample. Another group of objects characterized by very low luminosities are the so-called First Hydrostatic Cores (FHCs). FHCs were theoretically predicted by Larson (1969) and are supposed to form during the first stages of collapse, once the density is large enough to turn the collapse from isothermal to adiabatic, providing the required pressure to balance gravity. The predicted properties of FHCs are low internal luminosities (with bolometric luminosities $< 0.5 L_{\odot}$), very low masses ($0.04\text{--}0.1 M_{\odot}$, e.g., Boss & Yorke 1995; Saigo & Tomisaka 2006), Spectral Energy Distributions (SEDs) peaking around $100 \mu\text{m}$ (e.g., Omukai 2007) and association with low-velocity outflows (Machida et al. 2008). A number of FHC candidates actually present these properties (e.g., Onishi, Mizuno & Fukui 1999; Belloche et al. 2006; Enoch et al. 2010; Dunham et al. 2011; Pineda et al. 2011; Chen et al. 2010, 2012; Pezzuto et al. 2012; Murillo & Lai 2013; Hirano & Liu 2014). Thus, the properties of FHCs are similar to the properties expected for a deeply embedded Class 0-like proto-BD; it is the mass reservoir in the envelope (much larger for FHCs than for proto-BDs) that is the key distinguishing parameter between the two.

The number of proto-BD candidates proposed so far is very small. Barrado et al. (2009) and Palau et al. (2012) present a Class 0/I candidate of $0.003 L_{\odot}$, J041757B, associated with a possible thermal radiojet but with no molecular outflow detected so far (Phan-Bao et al. 2014). A more luminous Class 0/I candidate driving a compact outflow is L1148-IRS (Kauffmann et al. 2011), with $0.12 L_{\odot}$ and an envelope mass of $0.14 M_{\odot}$. Very recently, Lee et al. (2009, 2013) present a Class 0 object of $0.15 L_{\odot}$, driving an outflow and with an even smaller envelope mass, $0.09 M_{\odot}$, being thus the best proto-BD candidate known to date. With such a small number of proto-BD candidates, a primary urgent task is searching for further candidates in order to build a small sample and study whether their overall properties match the known relations of young stellar objects. In this work we present a new Class 0 proto-BD candidate driving a compact outflow and with only $0.03 M_{\odot}$ of envelope mass.

IC348-SMM2 is a submillimeter clump in the Perseus cloud at 240 pc of distance (Hirota et al. 2008, 2011; Chen et al. 2013). The clump, detected by Walawender et al. (2006)

using the James Clerk Maxwell Telescope (JCMT), is also detected with the Caltech Submillimeter Observatory (CSO) at $350 \mu\text{m}$ (Davidson et al. 2011) and *Herschel* (Sadavoy et al. 2014). At 1.3 mm, interferometric observations resolve the IC 348-SMM2 clump into two sources, a strong source driving a well-developed north-south outflow, also known as HH 797 (Pech et al. 2012; Chen et al. 2013), and a fainter object about 10 arcsec to the (north)east, referred to as ‘SMM2E’. Here we report on Submillimeter Array (SMA) observations which clearly show association of molecular gas with SMM2E, providing evidence that it belongs to IC 348. In addition, we complement the interferometric submillimetre data with new CSO observations and multiwavelength archive data that allow to gain insight into the nature of SMM2E.

2 OBSERVATIONS

2.1 SMA submillimetre data

The 345 GHz archive SMA (Ho et al. 2004) observations of the HH 797 outflow were carried out on 2006 Sep 8th in compact configuration, and with projected baselines ranging from 13 to 80 k λ . The phase reference centre for the observations was at RA(J2000.0) = 03:43:57.100, Dec(J2000.0) = +32:03:04.80. A mosaic of 7 pointings separated 17 arcsec in Dec was performed to cover a total field of view of roughly $3 \times 0.6 \text{ arcmin}^2$ oriented in the north-south direction and covering the strongest emission of the outflow. Receivers were tuned to cover the frequency range 345.589–347.589 GHz in the upper sideband (thus including the CO (3–2) line at 345.79599 GHz), and 335.589–337.589 GHz in the lower sideband. Channel spacing was set to 0.41 MHz (256 channels per chunk) across all the band, corresponding to a velocity resolution of 0.352 km s^{-1} . This was smoothed to 0.704 km s^{-1} . The FWHM of the primary beam at the frequency of observations is 37 arcsec.

Calibration was performed using the IDL superset MIR package¹ (Scoville et al. 1993) and following the standard procedures. Passband response was obtained from observations of PKS B1921–293, and 3C84 was used as a gain calibrator, for which typical rms of the phases were 55 per cent. The absolute flux density scale was determined from Uranus, and its uncertainty is estimated to be of 15–20 per cent. The positional accuracy is estimated to be ~ 0.3 arcsec.

Imaging was performed following the standard procedures in MIRIAD (Sault et al. 1995) and KARMA (Gooch 1996). A ROBUST (Briggs 1995) parameter equal to 2 was used to obtain a good sensitivity. The mosaic was corrected for the primary beam attenuation, with noise decreasing at the edges of the field of view. The resulting synthesized beam and rms noise of the continuum image are $2.81 \times 2.32 \text{ arcsec}^2$, P.A. = 87.37° , and 17 mJy beam⁻¹, and for the line we obtained a beam of $2.82 \times 2.32 \text{ arcsec}^2$, P.A. = 87.38° , and a rms noise of 0.8 Jy beam⁻¹ per channel.

In order to further study the CO (2–1), ¹³CO (2–1) and C¹⁸O (2–1) emission of SMM2E, we also imaged these transitions from the 230 GHz dataset published by Pech et al.

¹ The MIR-IDL cookbook by C. Qi can be found at <https://www.cfa.harvard.edu/~cqi/mircook.html>.

(2012). For CO (2–1), we selected a uv -range of 18–55 k λ , and used a robust parameter equal to -2 , yielding a final rms noise of $0.12 \text{ Jy beam}^{-1}$ per channel of 1.05 km s^{-1} width, and a synthesized beam of $3.14 \times 2.51 \text{ arcsec}^2$, P.A. = 86.05° . For ^{13}CO (2–1) and C^{18}O (2–1), we used a robust parameter equal to 0 (including the entire uv -range), yielding a final rms noise of $0.25 \text{ Jy beam}^{-1}$ per channel of 0.28 km s^{-1} width, and a synthesized beam of $3.64 \times 3.04 \text{ arcsec}^2$, P.A. = 83.44° , for ^{13}CO , and $3.56 \times 3.06 \text{ arcsec}^2$, P.A. = 87.37° , for C^{18}O .

2.2 CSO submillimetre data

IC 348-SMM2 was observed at the CSO in 2013 Nov 28 and 29 using the polarimeter for the Submillimeter High Angular Resolution Camera (SHARC-II, Dowell et al. 2003). SHARC-II is a camera of 32×12 pixels observing at $350 \mu\text{m}$, which can be used for polarization by placing a half-wave plate which is rotated at four different angles to determine the total flux and the linear polarization (Li et al. 2008). Although observations were carried out using the polarimeter, in this work we focus on the intensity image only of IC 348-SMM2. Observations were done in chop-nod mode, where an observation is made at each of the four half-wave plate angles, constituting one cycle. The target was observed for 27 half wave plate cycles (a single cycle takes about 7 minutes).

Opacities at 225 GHz were around 0.05 for both days. Neptune was observed for initial focus and pointing, and CRL 618 served for regular pointing corrections. The absolute flux scale was determined from L1551, for which we adopted a peak intensity of $45.2 \text{ Jy beam}^{-1}$. The uncertainty in the absolute flux scale is estimated to be ~ 30 per cent. The final map size and beam are $1.5 \times 1.5 \text{ arcmin}^2$ and 10 arcsec (FWHM), respectively. We followed the data reduction procedure as discussed in Davidson et al. (2011) and Chapman et al. (2013), achieving a rms noise near the map centre of 0.6 Jy beam^{-1} .

2.3 Ancillary data

We searched the Canada France Hawaii Telescope (CFHT), *Spitzer* and *Herschel* archives for images of the region and found that it was observed at several epochs in the optical and near-infrared (CFHT) as well as with *Spitzer* (Jørgensen et al. 2006; Rebull et al. 2007; Evans et al. 2009), and *Herschel*. Upper limits in the i , z , J , H , K_s bands were estimated by adding scaled Point Spread Functions (PSFs) of decreasing fluxes at the expected position of the source until the detection disappeared. The PSF used were taken from the images themselves, using a nearby point source with high signal-to-noise.

2.3.1 CFHT MegaCam

IC348-SMM2 was observed with *MegaCam* in the i and z bands in the course of programs 09BH43, 06BF29, 07BH50, and 13BD96. The individual pipeline processed images were retrieved from the Canadian Astronomy Data Center (CADC) archive. Individual exposures ranging from 3 to 300 s were obtained in each filter. The whole set of images

adds up to a total exposure time of 2990 s and 9201 s in the i and z -band, respectively. The individual frames were astrometrically and photometrically registered using SCAMP (Bertin 2006) and stacked using SWARP (Bertin et al. 2002).

2.3.2 CFHT WIRCam

IC348-SMM2 was observed with *WIRCam* in the J , H , and K_s broad-band filter and H_2 narrow-band filter. The individual pipeline processed and sky-subtracted images were retrieved from the CADC archive. Individual exposures ranging from 5 to 200 s were obtained. The whole set of images adds up to a total exposure time of 3710 s, 1360 s, 13455 s and 24810 s in the J , H , K_s and H_2 bands, respectively. The individual frames were astrometrically and photometrically registered using SCAMP and stacked using SWARP.

2.3.3 Herschel Space Observatory

The Perseus molecular clouds were observed by the *Herschel Space Observatory* as part of the Gould Belt Survey (André et al. 2010). A first set of observations was obtained in parallel mode using the PACS (70, 100, and $160 \mu\text{m}$) and SPIRE (250, 350, and $500 \mu\text{m}$) instruments simultaneously, but in this work we present the $100 \mu\text{m}$ data only from the Gould’s Belt project. More details about the observational strategy can be found in André et al. (2010). The *Herschel* images at 70 and $160 \mu\text{m}$ were obtained from the program GT2_zbalog_2 (P.I. Balog, integration time of 15792 s), for which observations were performed in scan mode. The data were pre-processed using the *Herschel* Interactive Processing Environment (Ott 2010) version 10.0.2843, and the latest available version of the calibration files. The final maps were subsequently produced using Scanamorphos version 21 (Roussel 2013), using its galactic option, as recommended to preserve large scale extended emission.

3 RESULTS

3.1 Continuum

In Fig. 1a we present the SMA $870 \mu\text{m}$ continuum emission (contours), overlaid on the H_2 $2.12 \mu\text{m}$ image from the CFHT archive (Section 2.3.2), showing the large-scale H_2 knots of the HH 797 outflow. The dominating submillimetre source in the field, SMM2 (Walawender et al. 2006), is the driving source of the large-scale outflow (e. g., Pech et al. 2012). In addition to SMM2, we detect $870 \mu\text{m}$ emission from SMM2E at about 10 arcsec to the northeast ($\sim 2400 \text{ AU}$). The source is detected up to 6 times the rms noise level and is unresolved (see zoom in Fig. 1b). This $870 \mu\text{m}$ source has a counterpart at 1.3 mm (detected with the SMA, Chen et al. 2013, who labelled the source ‘MMS2’) and at 2.1 cm (detected with the Jansky Very Large Array (JVLA) by Rodríguez et al. 2014, and labelled as ‘JVLA3c’).

Since SMM2E is unresolved by the SMA at $870 \mu\text{m}$, we adopt a flux density equal to the peak intensity, 0.11 Jy . Assuming a dust temperature of 24 K (see Section 4), and a dust mass opacity coefficient at $870 \mu\text{m}$ of $1.751 \text{ cm}^2 \text{ g}^{-1}$ (column 6 of Table 1 of Ossenkopf & Henning 1994, corresponding to agglomerated dust grains with thin ice mantles

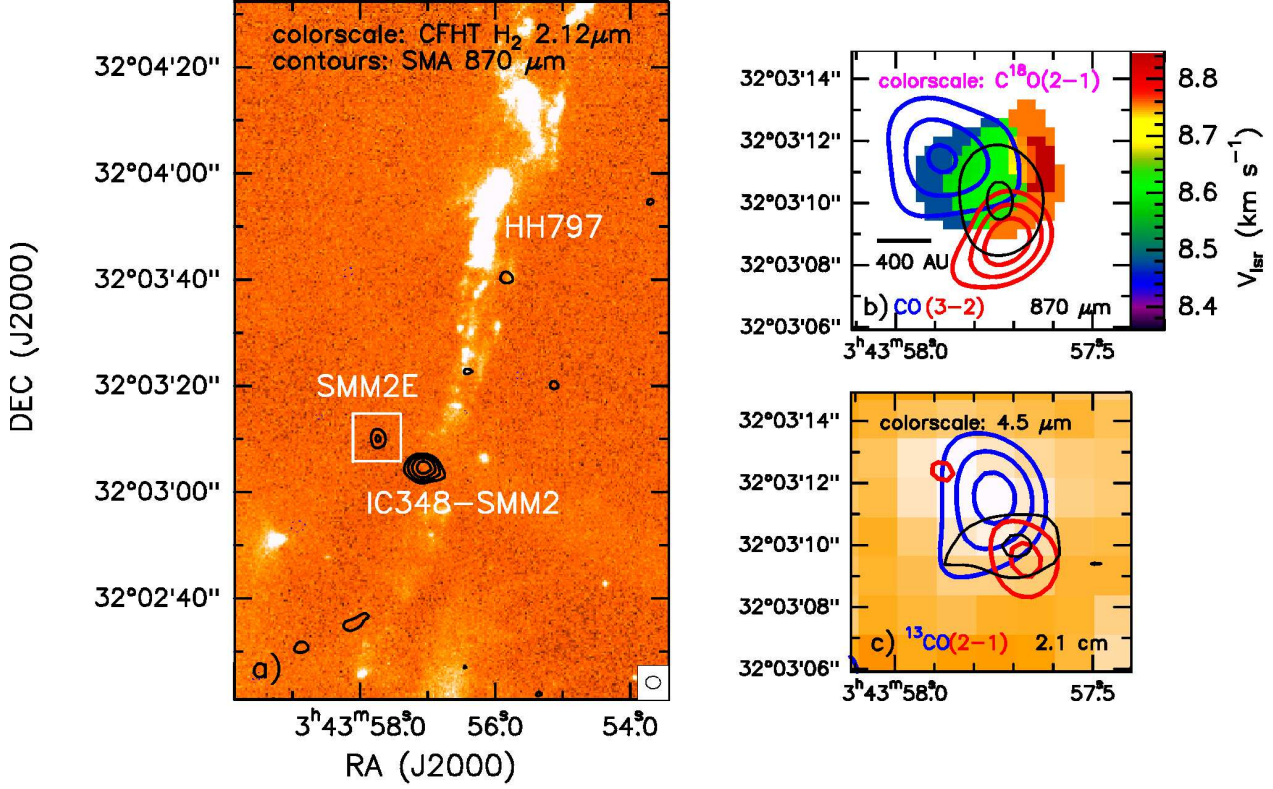


Figure 1. a) Large-scale field of view where IC348-SMM2 is found. Colorscale: CFHT H₂ archive image (Section 2.3.2). Black contours: SMA 870 μm continuum emission with contours -3 , 3 , 6 , 12 , and 24 times the rms noise of the map, 17 mJy beam^{-1} . b) Zoom in on SMM2E: SMA CO(3–2) blueshifted and redshifted emission (blue, red contours) and SMA 870 μm continuum (black contours, as in panel ‘a’). Blueshifted emission has been integrated from 4.0 to 6.1 km s^{-1} , while redshifted emission has been integrated from 9.7 to 11.1 km s^{-1} . Blue contours range from 21 to 99% of the peak intensity ($42.9 \text{ Jy beam}^{-1} \text{ km s}^{-1}$), increasing in steps of 15% . Red contours range from 15 to 99% of the peak intensity ($33.8 \text{ Jy beam}^{-1} \text{ km s}^{-1}$), increasing in steps of 5% . The colorscale is the first-order moment of the C¹⁸O(2–1) emission showing a velocity gradient perpendicular to the outflow. c) Zoom in on SMM2E: SMA ¹³CO(2–1) emission (blue contours correspond to the 9.0 km s^{-1} velocity, and red contours correspond to the 12.9 km s^{-1} velocity) and VLA 2.1 cm continuum emission (black contours, Rodríguez et al. 2014). Blue contours range from 37 to 99% of the peak intensity ($1.43 \text{ Jy beam}^{-1} \text{ km s}^{-1}$), increasing in steps of 15% . Red contours range from 37 to 99% of the peak intensity ($0.89 \text{ Jy beam}^{-1} \text{ km s}^{-1}$), increasing in steps of 10% . Black contours (2.1 cm) range from -3 , 3 , and 6 times the rms noise of the map, $4.7 \mu\text{Jy beam}^{-1}$. The colorscale is the Spitzer/IRAC2 image showing a brightness increase at the position of the blueshifted lobe.

Table 1. Parameters of the $870 \mu\text{m}$ continuum sources detected with the SMA

Source	Position ^a		Dec. ang. size ^a ($'' \times ''$)	Physical size ^a (AU \times AU)	Dec. P.A. ^a ($^\circ$)	J_ν^{peak} ^a (Jy beam ⁻¹)	S_ν ^a (Jy)	Mass ^b (M_{Jup})
	α (J2000)	δ (J2000)						
SMM2	03:43:57.06	32:03:04.6	2.20×1.74	530×420	75.8	0.610 ± 0.017	0.97 ± 0.19	250
SMM2E	03:43:57.73	32:03:10.1	$< 1.4 \times 1.1$	$< 340 \times 260$	-	0.113 ± 0.017	0.11 ± 0.02	29

^a Position, deconvolved size, peak intensity, and flux density are derived by fitting a Gaussian in the image domain. Uncertainty in the peak intensity is the rms noise of the cleaned image, σ . Uncertainty in flux density has been calculated as $\sqrt{(\sigma \theta_{\text{source}}/\theta_{\text{beam}})^2 + (\sigma_{\text{abs}})^2}$ (Beltrán et al. 2001), where θ_{source} and θ_{beam} are the size of the source and the beam respectively, and σ_{abs} is the error in the absolute flux scale, which takes into account the uncertainty on the calibration applied to the flux density of the source ($S_\nu \times \%\text{uncertainty}$).

^b Masses derived assuming a dust temperature of 24 K (Section 4), and a dust (and gas) mass opacity coefficient of $0.0175 \text{ cm}^2 \text{ g}^{-1}$ (obtained by interpolating the tabulated values of Ossenkopf & Henning 1994, see Section 3.1). The uncertainty in the masses due to the opacity law is estimated to be a factor of 2 (Ossenkopf & Henning 1994).

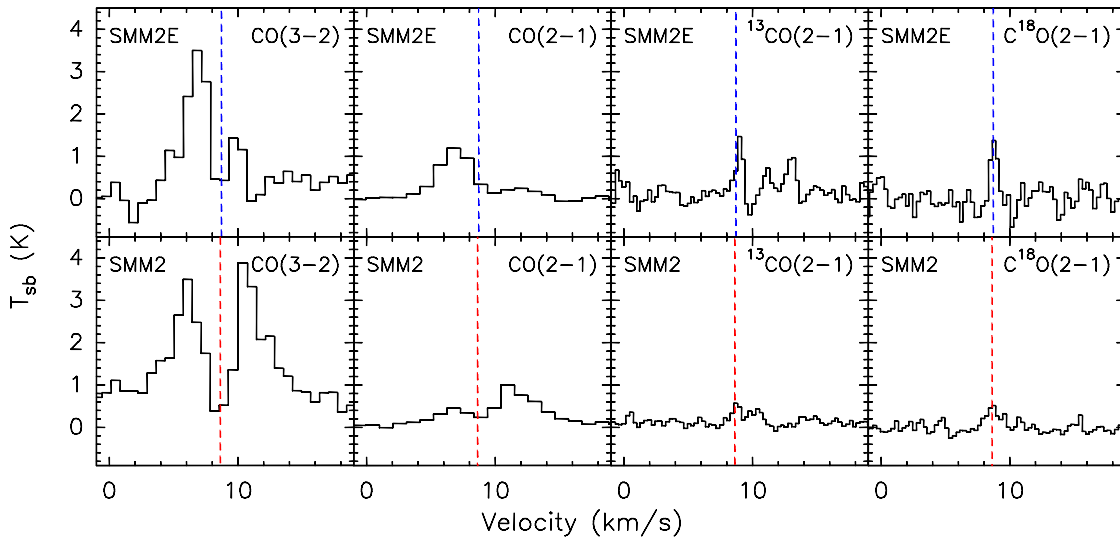


Figure 2. *Top, from left to right:* CO(3–2), CO(2–1), ^{13}CO (2–1), and C^{18}O (2–1) spectra for SMM2E, averaged over a polygon of ~ 8 arcsec of diameter centred on the source. *Bottom, from left to right:* idem for SMM2, averaging over a polygon of 8×14 arcsec 2 . Vertical dashed lines indicate the v_{lsr} for SMM2E (~ 8.72 km s $^{-1}$) and for SMM2 (~ 8.63 km s $^{-1}$) measured in the C^{18}O spectra.

at densities $\sim 10^6$ cm $^{-3}$), the flux density measured with the SMA corresponds to a total mass of gas and dust of $\sim 30 M_{\text{Jup}}$. We estimated an uncertainty in the masses due to uncertainty in the dust opacity of about a factor of 2 (Ossenkopf & Henning 1994). The positions, deconvolved sizes, peak intensities, flux densities and mass estimates of both SMM2 and SMM2E are listed in Table 1.

3.2 Molecular line data

Spectra of the average emission inside a polygon of ~ 8 arcsec of diameter (8×14 arcsec 2) centred on SMM2E (SMM2) are shown in Fig. 2 for CO(3–2), CO(2–1), ^{13}CO (2–1) and C^{18}O (2–1). The CO(3–2) spectra for both SMM2E and SMM2 show a double-peaked profile which could be due in part to the filtering of emission at systemic velocities and/or self-absorption of the cold foreground cloud. However, while the blueshifted and redshifted wings have similar intensities for SMM2, this is not the case of SMM2E, for which the peak of emission is found at 6.8–7.5 km s $^{-1}$. For these velocities, the emission of SMM2E dominates over the emission of the SMM2 outflow (within one primary beam), and consists of one main lobe elongated roughly in the east-west direction. It also presents some deep negative features which probably arise from large-scale emission filtered out by the SMA (see channel maps in Fig. A1 of the Appendix). This suggests that the emission at these velocities traces part of the large-scale ambient cloud. The CO(2–1) and ^{13}CO (2–1) spectra towards SMM2E indicate that the CO(2–1) emission is optically thick (opacity ~ 18), as the intensity of the CO(2–1) is only a factor of 4 larger than the intensity of ^{13}CO (2–1) (once smoothed to the same spectral resolution, and assuming a $^{12}\text{CO}/^{13}\text{CO}$ ratio of 65, Chin et al. 1995). For this reason, we refrain from studying the outflow using CO(2–1), and rather present the emission traced by ^{13}CO (2–1) at two particular velocities (systemic, and redshifted), showing one lobe to the north(east) and another fainter lobe to the

south(west) of SMM2E (see Fig. 1c). On the other hand, the C^{18}O (2–1) line from SMM2E is narrow (0.67 km s $^{-1}$ of line width), and can be used to infer the systemic velocity of SMM2E, which is found to be very similar to the systemic velocity of SMM2 (8.72 and 8.63 km s $^{-1}$, respectively, after gaussian fitting of the spectra). Concerning the morphology of the C^{18}O (2–1) emission associated with SMM2E, shown in Fig. 1b, it is compact and presents a velocity gradient in the (south)east-(north)west direction (see also the channel maps in Fig. A2 of the Appendix).

Fig. 1b presents the zero-order moments of the CO(3–2) emission, revealing a blueshifted compact lobe to the north(east) and a redshifted compact lobe to the south(west) of SMM2E, similar to what is seen in ^{13}CO (2–1) (Fig. 1c). Blueshifted emission in SMM2E is stronger than redshifted emission, and ranges from 4 to 6.5 km s $^{-1}$, while the redshifted emission ranges from 9.7 to 11 km s $^{-1}$. The blueshifted lobe is separated from the redshifted lobe by 3–4 arcsec, or 700–1000 AU, and the blueshifted lobe size is 2–3 arcsec (~ 600 AU) while the red lobe is unresolved. Furthermore, the blueshifted lobe matches a 4.5 μm brightness increment as seen with *Spitzer* (see Fig. 1c). The redshifted lobe is more compact and fainter than the blueshifted one. This difference, which has been seen in other cases (e.g., Pety et al. 2006; Fernández-López et al. 2013) and is predicted by simulations (e.g., Offner et al. 2011), could be due to the fact that the redshifted emission is located towards the southwest, where the extinction (and opacity) increases because of the extended envelope of SMM2.

We derived the CO(3–2) column density (from the 8 arcsec averaged spectrum, Fig. 2) following Palau et al. (2007, 2013). To do this, we first estimated the excitation temperature assuming optically thick emission in the line centre (see Table 2), and calculated the line area for the velocity ranges where the outflow wings are detected (given in Fig. 1). We used an opacity correction factor for CO(3–2) of ~ 10 , adopted to be smaller than the mea-

Table 2. Physical parameters of the CO (3–2) outflow driven by SMM2E

Lobe	t_{dyn} (yr)	dec. size (arcsec)	N_{12} ^a (cm^{-2})	M_{out} ^a (M_{\odot})	\dot{M} ^a ($M_{\odot} \text{ yr}^{-1}$)	P ^a ($M_{\odot} \text{ km s}^{-1}$)	\dot{P} ^a ($M_{\odot} \text{ km s}^{-1} \text{ yr}^{-1}$)	E_{kin} ^a (erg)	L_{mech} ^a (L_{\odot})
Red	670	$< 1.4 \times 1.1$	1.1×10^{16}	5.3×10^{-6}	7.8×10^{-9}	7.4×10^{-6}	1.1×10^{-8}	1.0×10^{38}	7.4×10^{-7}
Blue	530	2.2×1.1	3.8×10^{16}	2.8×10^{-5}	5.3×10^{-8}	5.9×10^{-5}	1.1×10^{-7}	1.2×10^{39}	8.6×10^{-6}
All	600	–	4.9×10^{16}	3.3×10^{-5}	5.6×10^{-8}	6.7×10^{-5}	1.1×10^{-7}	1.3×10^{39}	9.3×10^{-6}

^a Parameters are calculated following Palau et al. (2007, 2013), without correcting for inclination. From the line peak of the CO (3–2) spectrum, ~ 3.5 K, we estimated an excitation temperature of ~ 10 K, assuming optically thick emission in the line centre. The CO (3–2) outflow parameters were corrected for opacity using a correction factor of 10, taken as a first approach from the facts that the opacity of CO (2–1) is measured to be ~ 18 (see Section 3.2), and that CO (3–2) is typically optically thinner than CO (2–1).

Table 3. Photometry for SMM2E

λ (μm)	S_{ν} (mJy)	σ_{abs} ^a (mJy)	Beam (arcsec)	Instrument
0.75	< 0.00049	–	–	CFHT/Megacam
0.88	< 0.00062	–	–	CFHT/Megacam
1.25	< 0.0098	–	–	CFHT/WIRCAM
1.62	< 0.021	–	–	CFHT/WIRCAM
2.13	< 0.016	–	–	CFHT/WIRCAM
3.6 ^b	< 0.0026	–	1.7	Spitzer/IRAC
4.5 ^b	0.021	0.006	1.7	Spitzer/IRAC
5.8 ^b	0.10	0.04	1.9	Spitzer/IRAC
8.0 ^b	0.16	0.10	2.0	Spitzer/IRAC
24 ^b	3.2	0.4	6.0	Spitzer/MIPS
70	360	50	5.6	Herschel/PACS
100	1200	100	6.8	Herschel/PACS
160	1300	700	11	Herschel/PACS
350	1400	600	10	CSO
450	1000	400	9	JCMT
850	110	20	2.8×2.3	SMA
1300 ^b	65	15	3.3×3.0	SMA
21000 ^b	0.027	0.008	2.4×1.7	JVLA
33000 ^b	< 0.016	–	3.9×2.5	JVLA

^a Absolute flux uncertainty as described in Table 1.

^b The measurements of Spitzer/IRAC+MIPS, SMA at 1.3 mm, and JVLA at 2.1 and 3.3 cm are reported in Evans et al. (2009), Chen et al. (2013) and Rodríguez et al. (2014).

sured opacity for CO (2–1) (~ 18 , see above). The resulting CO column density is $\sim 5 \times 10^{16} \text{ cm}^{-2}$. As for the mass, we used the (deconvolved) sizes given in Table 2, adopted a mean molecular weight of 2.8, and a CO abundance of $X(^{12}\text{CO})=10^{-4}$ (e.g., Frerking, Langer, & Wilson 1982), obtaining a final (blueshifted + redshifted lobes) mass of $3 \times 10^{-5} M_{\odot}$. The outflow parameters given in Table 2 were estimated also following Palau et al. (2007), and without correcting for inclination. We obtained a mass outflow rate of $6 \times 10^{-8} M_{\odot} \text{ yr}^{-1}$, an outflow force of $10^{-7} M_{\odot} \text{ km s}^{-1} \text{ yr}^{-1}$, and a mechanical luminosity of $\sim 10^{-5} L_{\odot}$ (Table 2).

4 ANALYSIS

4.1 Building the SED for SMM2E

With the aim of building the SED and estimating the bolometric luminosity of SMM2E, we used the archive data reported in Section 2.3. While the object remains undetected in the CFHT and Spitzer/IRAC1 bands, there are detections in IRAC2, IRAC3, IRAC4, MIPS1 (fluxes reported in Evans et al. 2009) and Herschel/PACS bands, which we present in Fig. 3. It is worth noting that IRAC3, IRAC4 and MIPS1 images also reveal an elongated structure oriented in the southeast-northwest direction and passing through SMM2E (Fig. 3b–d).

Regarding the *Herschel*/PACS bands, at $70 \mu\text{m}$ SMM2E is well separated from SMM2 (Fig. 3e). In order to estimate the flux of SMM2E at $70 \mu\text{m}$, we convolved the PSF of PACS at $70 \mu\text{m}$ by a Gaussian² (to take into account the possible contribution of the PSF side lobes and the extended emission from SMM2 to SMM2E), and subtracted the convolved PSF from the observed image. The residual image presents a clear excess of emission at the position of SMM2E, and we fitted such an excess with a Gaussian + constant level, providing us with the flux for SMM2E at this wavelength (Table 3). Uncertainties were estimated by using different boxes for the Gaussian + constant level fit. We estimated the fluxes of SMM2E at 100 and 160 μm (Figs. 3f,g) by applying the same technique.

In panel ‘h’ of Fig. 3 we present the CSO 350 μm continuum emission of the observations described in Section 2.2. The morphology of the emission is fully consistent with the results obtained by Davidson et al. (2011), with the difference that our image is calibrated in absolute flux scale. We fitted a Gaussian + constant level in a region including only the western part of SMM2, and the residual image presents an excess at the position of SMM2E, of 1.4 Jy beam^{-1} . At slightly longer wavelengths, we used the 450 μm image of Walawender et al. (2006, see Fig. 3i) to fit a Gaussian + constant level as in the CSO image. The residual shows an excess of emission up to 1.0 Jy beam^{-1} at the position of SMM2E, and we adopt this value to build the SED. Finally, we also used the values measured with the SMA at 870 μm (this work), 1.3 mm (Chen et al. 2013), and the value at 2.1 cm (Rodríguez et al. 2014). In Table 3 we list the mea-

² The Gaussian size for the convolution was estimated from a Gaussian fit to the $70 \mu\text{m}$ emission in SMM2.

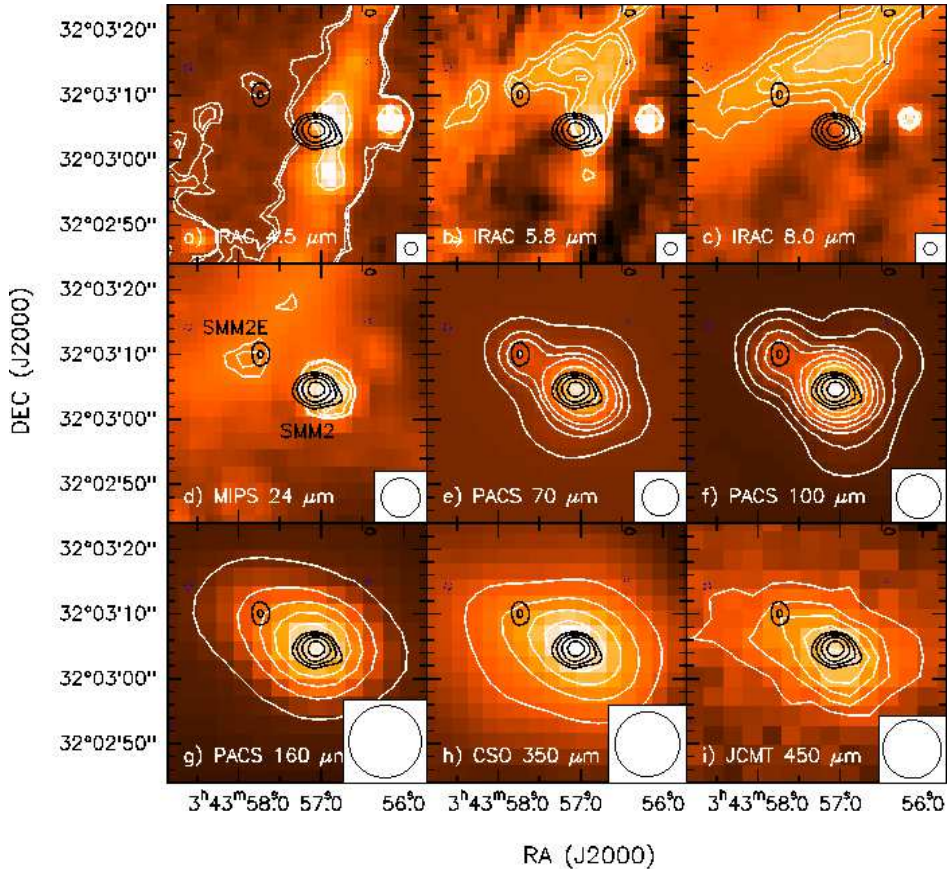


Figure 3. Color scale and white contours: emission at different wavelengths from 4.5 to 450 μm in the field of view of SMM2. Contours are: panel ‘a’ (IRAC 4.5 μm): 0.48, 0.50, 1.1, and 1.8 MJy sr^{-1} ; panel ‘b’ (IRAC 5.8 μm): 5.3, 5.4, and 5.5 MJy sr^{-1} ; panel ‘c’ (IRAC 8.0 μm): 17.0, 17.3, 17.6, and 17.9 MJy sr^{-1} ; panel ‘d’ (MIPS 24 μm): 43.4, 43.6, 44.5, 45.5, and 46.5 MJy sr^{-1} ; panel ‘e’ (PACS 70 μm): 0.15, 0.30, 0.45, 0.65, 1.2, 2.0, and 3.0 Jy beam^{-1} ; panel ‘f’ (PACS 100 μm): 1.0, 1.5, 2.5, 3.5, 5.0, 7.0, and 9.0 Jy beam^{-1} ; panel ‘g’ (PACS 160 μm): 3, 6, 9, 12, 15, and 18 Jy beam^{-1} ; panel ‘h’ (CSO 350 μm): 4.8, 5.9, 7.1, 8.3, and 9.5 Jy beam^{-1} ; panel ‘i’ (JCMT 450 μm): 0.25, 0.75, 1.25, 1.75, and 2.5 Jy beam^{-1} . In all panels, black contours correspond to the SMA 870 μm emission (contours as in Fig. 1), and the beam is shown in the bottom right corner of each panel.

sured fluxes (or upper limits) for SMM2E at different wavelengths.

4.2 SED properties

By using the flux measurements estimated in the previous section we built the SED of SMM2E (Fig. 4). The SED peaks near 100 μm and decreases about two orders of magnitude at near-infrared wavelengths, with no flatness in the mid-infrared range. This is not seen in more evolved objects which have already been detected in the near-infrared, such as the proto-BD candidates J041757B (Barrado et al. 2009; Palau et al. 2012) and L328-IRS (Lee et al. 2009, 2013). The SEDs of these two objects are also shown in Fig. 4 for comparison, and both present brighter fluxes in the near/mid-infrared than SMM2E, while the submillimetre fluxes are comparable.

A fit of a modified black-body to the SED of SMM2E (red dashed line in Fig. 4) can account for all the measured fluxes from 70 μm down to the centimetre range, within uncertainties. Thus, the SED of SMM2E is typical of ‘early’ Class 0 young stellar objects (e.g., Enoch et al.

2009). From these data we estimated a bolometric temperature for SMM2E of ~ 35 K, which falls within the range of values of Class 0 objects ($T_{\text{bol}} < 70$ K; Chen et al. 1995). To do the fit of the modified black body, we used two methods. First, we searched for the parameters minimizing the χ^2 in the ranges $10 \leq T_{\text{d}} \leq 35$ K (by steps of 1 K), $5 \leq M_{\text{env}} \leq 60 M_{\text{Jup}}$ (by steps of 5 M_{Jup}), and $0.1 \leq \beta \leq 1.5$ (by steps of 0.1), and found the minimum χ^2 for a dust temperature of 24 K, an envelope mass of 35 M_{Jup} , and a dust emissivity index of 0.8 (adopting the same opacity at 870 μm as in Section 3, and assuming that the opacity changes with frequency following a power law of index β). Second, we performed a Bayesian analysis by comparing the SED of the target with the grid of 2574 modified blackbody models covering the ranges given above. For each model, the reduced χ^2 and corresponding relative probability $e^{-\chi^2/2}$ were computed. The relative likelihood for each of the parameters was obtained by a marginalization of the parameter space successively over each dimension. Figure 5 shows the corresponding probability density functions, from which we derived the most probable values. Uncertainties on these values were estimated using bootstrapping and computing the

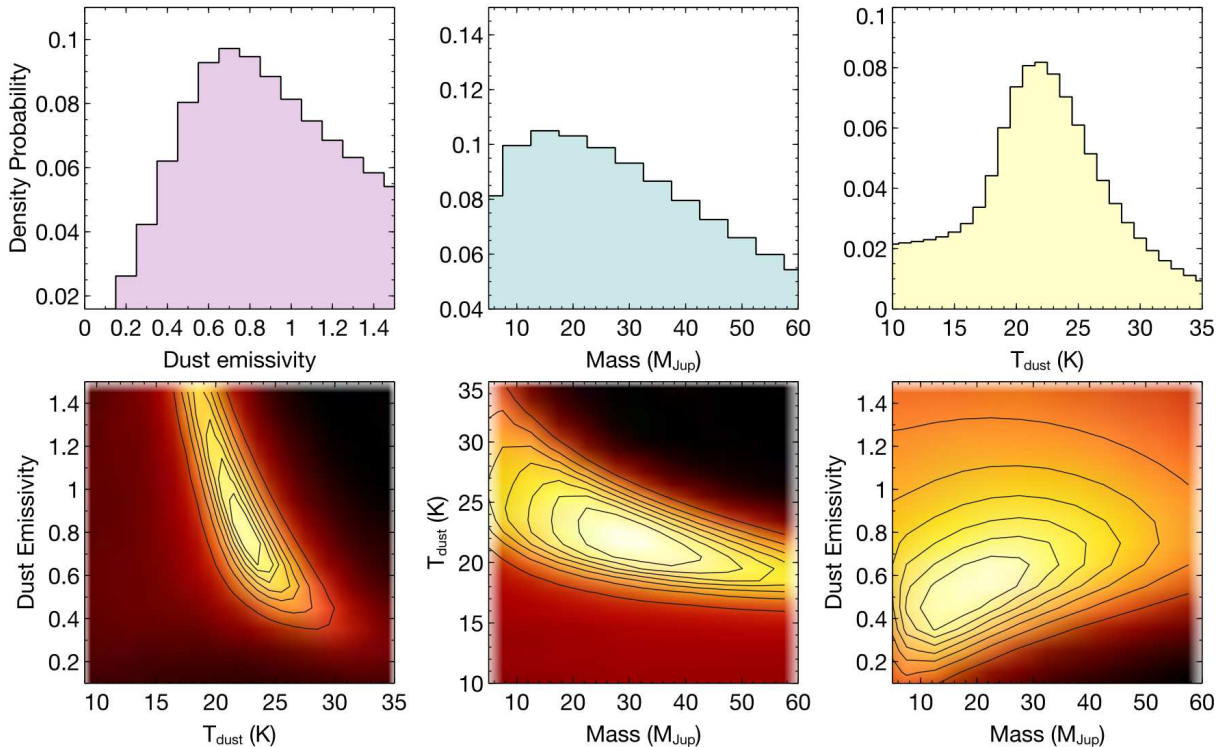


Figure 5. Top: Probability density functions of the three parameters of the modified blackbody fit (shown in Fig. 4 with a red dashed line). Bottom: χ^2 maps of the fit for the different pairs of parameters.

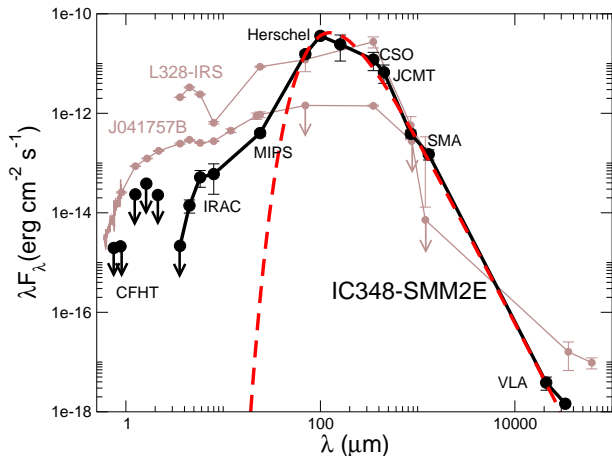


Figure 4. SED of IC348-SMM2E (black thick solid line) compared to two previously reported proto-BD candidates (brown thin solid lines), J041757-B (Barrado et al. 2009; Palau et al. 2012) and L328-IRS (Lee et al. 2009, 2013). The SED suggests that SMM2E is a more embedded object than the other proto-BDs, being a SED typical of Class 0 low-mass protostars. The dashed (red) line shows the fit of a modified blackbody of 24 K, $35 M_{\text{Jup}}$, and dust emissivity index of 0.8.

2.5% and 97.5% confidence interval over 1000 replications. The Bayesian analysis yields that the most probable values of the parameters are: $22 +2/-2$ K, $15 +15/-5 M_{\text{Jup}}$, and $0.7 +0.3/-0.1$, for the dust temperature, envelope mass and dust emissivity index, respectively. These values are in good agreement with the values minimizing χ^2 , with the envelope mass slightly shifted towards lower masses.

5 DISCUSSION

5.1 Will SMM2E remain substellar?

From the SED presented in the previous section, we estimate a bolometric luminosity for SMM2E of $0.10 L_{\odot}$. This bolometric luminosity already classifies SMM2E as a VeLLO. In addition, SMM2E is not likely a young stellar object in a quiescent phase because the mechanical luminosity estimated from the outflow is $\sim 10^{-5} L_{\odot}$ (Section 3.2), much smaller than the bolometric luminosity.

The measured bolometric luminosity is an upper limit to the internal luminosity of the object, because part of the luminosity might be produced by the interstellar radiation field. A first approach to the internal luminosity of an object can be obtained if the flux at $70 \mu\text{m}$ is known (Dunham et al. 2008). Using equation (2) of Dunham et al. (2008), and for the flux measured by us at $70 \mu\text{m}$ (Section 4) we obtain an internal luminosity for SMM2E of $0.06 L_{\odot}$, corresponding to a mass of $\sim 75 M_{\text{Jup}}$ according to the evolutionary models of Baraffe et al. (2002, Fig.2), and for the earliest possible time computed for these models (1 Myr). The accreted mass of the central object is probably smaller than

75 M_{Jup} because for Class 0 objects the envelope mass is comparable to the accreted mass (e.g., André et al. 1993; Dunham et al. 2008), and for the envelope mass we estimated a value $\lesssim 35 M_{\text{Jup}}$ (Sections 3 and 4). In addition, part of the internal luminosity might come from accretion.

An independent estimate of the stellar mass can be made assuming that the internal luminosity arises entirely from accretion (a reasonable assumption for Class 0 objects). Assuming the Shu (1977) model, the mass accretion rate at which an initially isothermal core accretes, \dot{M}_{acc} , depends only on the sound speed c_s : $\dot{M}_{\text{acc}} = \frac{\eta_{\dot{M}}}{G} c_s^3$, where G is the gravitational constant and $\eta_{\dot{M}}$ is the efficiency in the mass accretion rate. Thus, \dot{M}_{acc} can be written in terms of the initial temperature of the core as $\dot{M}_{\text{acc}} = \frac{\eta_{\dot{M}}}{G} \left(\frac{kT}{\mu m_{\text{H}}} \right)^{3/2}$.

On the other hand, the accretion luminosity is directly proportional to the mass accretion rate:

$$L_{\text{acc}} = \eta_{\text{L}} \frac{G m_* \dot{M}_{\text{acc}}}{R_*}, \quad (1)$$

where η_{L} is the accretion luminosity efficiency with respect to steady spherical infall (for steady accretion through an optically thick disk, $\eta_{\text{L}} \sim 1/2$, Hartmann 1998), and m_* and R_* are the mass and radius of the central hydrostatic object. Thus, L_{acc} and m_* are related linearly and m_* can be written in the form:

$$m_* = L_{\text{acc}} \frac{R_*}{\eta_{\text{L}} \eta_{\dot{M}}} \left(\frac{\mu m_{\text{H}}}{kT} \right)^{3/2}. \quad (2)$$

We assumed $\eta_{\dot{M}} \sim 0.1$ (Terebey et al. 2006; Myers 2014), and an initial gas temperature T around 10 K, which corresponds to a mass accretion rate of $\sim 1.6 \times 10^{-7} M_{\odot} \text{yr}^{-1}$, only a factor of two larger than the mass outflow rate inferred for SMM2E (see Table 2). For the radius R_* , we adopted a range from 0.1 R_{\odot} (for pre-main sequence brown dwarfs, Stassun et al. 2012; Sorahana et al. 2013) to 1 R_{\odot} (from the simulations following the collapse of a core to stellar densities, yielding about $< 3 R_{\odot}$ for the second hydrostatic core for a collapsing core of 1 M_{\odot} , Bate, Tricco & Price 2014). For this range of values, and assuming that the internal luminosity comes from accretion (to be conservative), we obtain that m_* ranges from 2 to 24 M_{Jup} , well within the brown dwarf domain. This accreted mass is fully consistent with the dynamical mass estimated from the C^{18}O (2–1) velocity gradient shown in Fig. 1b, of 16 M_{Jup} . The velocity gradient is seen perpendicular to the outflow and thus could be tracing rotation of an envelope/disk of about 300 AU of radius. If confirmed, this would be the first disk found around a Class 0 proto-BD.

The reservoir of mass still available in the envelope is $\lesssim 35 M_{\text{Jup}}$ (Section 4.2). This is comparable to the mass which should be accreted in the future assuming that the object will continue accreting at the same rate during the typical timescale of the Class 0 phase, $(5\text{--}10) \times 10^4$ yr (e.g., Froebrich et al. 2006; Evans et al. 2009; Enoch et al. 2009; Dunham & Vorobyov 2012). Thus, the final mass should be the sum of the current mass (2 to 24 M_{Jup}) plus the mass which will be accreted in the future ($\lesssim 35 M_{\text{Jup}}$), which corresponds to a final mass $< 59 M_{\text{Jup}}$. Therefore, the true final mass of SMM2E will most likely remain substellar.

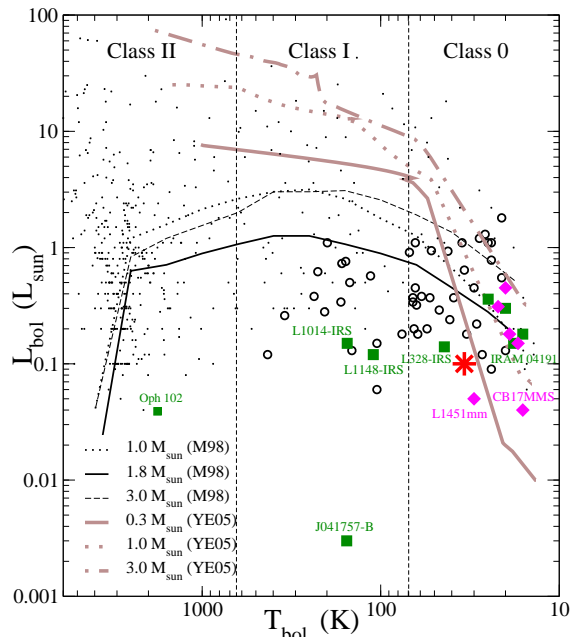


Figure 6. Bolometric luminosity vs. bolometric temperature diagram after Young & Evans (2005), Dunham et al. (2008) and Barrado et al. (2009). The 50 sources compiled by Dunham et al. (2008), showing some evidence for being embedded low luminosity sources, are shown as empty black circles. The thick brown lines correspond to the evolutionary tracks for the three models with different masses (in solar masses) considered by Young & Evans. (2005). The thin black lines show the evolutionary tracks for three models considered by Myers et al. (1998). The dots correspond to Taurus members and the vertical dashed lines show the Class 0/I and Class I/II T_{bol} boundaries from Chen et al. (1995). VeLLOs are marked as green squares, FHCs are marked as magenta diamonds, and SMM2E is shown as a large red asterisk (see Table 4).

5.2 Comparison of SMM2E with other proto-BD candidates and young stellar objects

Since the discovery of VeLLOs (Young et al. 2004), a number of objects with bolometric luminosities $\lesssim 0.5 L_{\odot}$ have been studied in detail and have been found to be driving outflows. In Table 4 we compile the main properties of the most studied VeLLOs and FHCs. However, in most of the cases the available mass reservoir is large enough to cast doubt on the final substellar nature of the objects. In addition, their SEDs present different shapes suggestive of different evolutionary stages.

To visualize this more clearly, in Fig. 6 we plot the position of VeLLOs (green squares) and FHCs (magenta diamonds) in a L_{bol} vs T_{bol} diagram. The figure shows that SMM2E is the least luminous of the Class 0 VeLLOs, and in Table 4 we show that it is associated also with the least massive envelope. Only L328-IRS (Lee et al. 2009, 2013) has L_{bol} , T_{bol} , and envelope mass comparable to those in SMM2E. These two objects are very similar, not only in

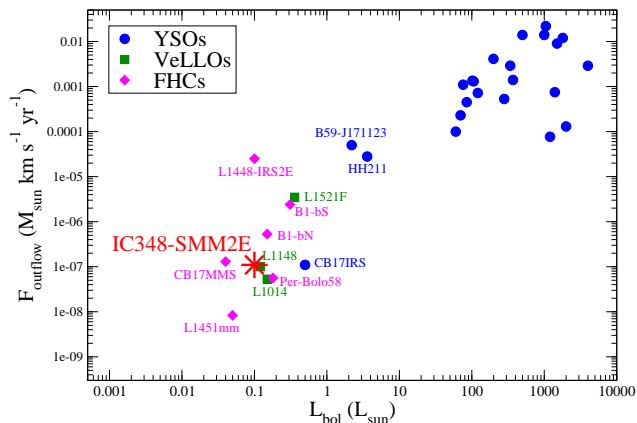


Figure 7. Comparison of outflow force vs bolometric luminosity for objects observed with mm/submm interferometers. Blue dots correspond to young stellar objects (YSOs) from Beltran et al. (2008), Palau et al. (2006), Chen et al. (2012), Hara et al. (2013) and Duarte-Cabral et al. (2013). Green squares correspond to Very Low Luminosity Objects (VeLLOs), and magenta diamonds correspond to First Hydrostatic Cores (FHCs, see references in Table 4). The red asterisk corresponds to SMM2E (this work).

the properties of their SEDs, but also in the velocity extension of their outflows, of $\sim 2 \text{ km s}^{-1}$ wide. The main difference between SMM2E and L328-IRS is the outflow size. The SMM2E outflow has not been detected in single-dish observations, and the interferometric images reveal lobes of only $\sim 500 \text{ AU}$ (Table 2), while the outflow driven by L328-IRS extends up to $\sim 20000 \text{ AU}$, indicating a longer lifetime. The fact that the mid-infrared fluxes of SMM2E are much lower than the L328-IRS fluxes (Fig. 4) also indicates that SMM2E is probably younger than L328-IRS. Regarding the FHCs, there are only two with lower luminosity than that of SMM2E, L1451mm (Pineda et al. 2011), and CB17-MMS (Chen et al. 2012). The mass reservoir (estimated from single-dish) of CB17-MMS is of the order of $\sim 1 M_{\odot}$ (Launhardt et al. 2010), being easy for CB17-MMS to achieve stellar masses. On the other hand, the outflow lobes of L1451mm are very compact, $\sim 500 \text{ AU}$, and the outflow velocities cover only $\lesssim 2 \text{ km s}^{-1}$ (Pineda et al. 2011), comparable to those in SMM2E. However, the mass reservoir of L1451mm is five times larger than that of SMM2E (Table 4). Thus, SMM2E turns to be among the youngest Class 0 proto-BD candidates with a substellar-mass envelope.

There are a number of well-known correlations established for large samples of young stellar objects. If BDs form as a scaled-down version of low-mass stars, we expect that the properties of proto-BDs should fit also in these correlations. In particular, the outflow force seems to correlate with the bolometric luminosity of the driving source (e.g., Bon-temps et al. 1996; Wu et al. 2004; Takahashi & Ho 2012). In Fig. 7 we plot the outflow force of SMM2E and its bolometric luminosity on data from the literature of outflows observed with interferometers (using similar configurations), in order to avoid estimates of the missing flux which are necessarily

uncertain. For the low and intermediate-mass young stellar objects, we used the compilation by Beltran et al. (2008), and added the works of Palau et al. (2006), Chen et al. (2012), Hara et al. (2013), and Duarte-Cabral et al. (2013). For the lower mass objects we mainly included the VeLLOs and FHCs whose outflow has been detected with an interferometer³ (L1521F: Bourke et al. 2006, Takahashi et al. 2013; L1148-IRS: Kauffmann et al. 2011; L1014-IRS: Bourke et al. 2005, Maheswar et al. 2011; L1448-IRS2E: Chen et al. 2010; Per-Bolo58: Enoch et al. 2010, Dunham et al. 2011; L1451mm: Pineda et al. 2011; CB17-MMS and CB17-IRS: Chen et al. 2012). The figure shows that SMM2E falls on the expected position in this diagram if one extrapolates the trend traced by the sample of young stellar objects (blue dots). Thus, SMM2E seems to behave as a scaled-down version of low-mass stars, and probably will keep its mass substellar, constituting one of the few examples of an excellent Class 0 proto-BD candidate.

5.3 Is SMM2E forming isolated? A possible wide triple system

In the previous section we showed that SMM2E seems to be a proto-BD candidate forming as a scaled-down version of low-mass stars. Something which remains to be answered however is whether SMM2E is forming isolated or is a companion of SMM2. In the 5.8, 8.0 and 24 μm images there is an extended structure elongated in the southeast-northwest direction and SMM2E lies in its southern tip (see Fig. 3b,c,d). This structure is reminiscent of the ‘striations’ seen near filaments in both high-mass and low-mass star-forming clouds (e.g., Goldsmith et al. 2008; Busquet et al. 2013; Palmeirim et al. 2013). However, SMM2E could just fall in projection at the tip of the striation. In addition, this striation is not seen in any of the Herschel bands, suggesting it must be relatively warm, and such a warm structure is not expected to fragment into substellar mass fragments, making this possibility unlikely.

Another possibility is that SMM2E is gravitationally bound to SMM2. SMM2 is a Class 0 young stellar object for which a bolometric luminosity of 0.4–1.1 L_{\odot} is measured (e.g., Hatchell et al. 2007⁴; Enoch et al. 2009). If we assume that this bolometric luminosity comes from accretion, and use equation (2) (for a radius similar to the solar radius), we obtain an accreted mass for SMM2 of 0.2–0.4 M_{\odot} . On the other hand, the difference of peak (radial) velocities of SMM2E and SMM2 seen in the C^{18}O (2–1) spectra is around $\sim 0.1 \text{ km s}^{-1}$, which is consistent with a mass for SMM2 of $\lesssim 0.4 M_{\odot}$ if SMM2E is orbiting around SMM2. Thus it seems plausible that both objects constitute a multiple system. Actually, Rodríguez et al. (2014) show that SMM2 seems to be a binary itself, making this group of objects a possible triple system, with very wide separations of 720 and

³ We did not include low-luminosity objects whose SED resembles those of Class II YSOs, likely corresponding to later evolutionary stages compared to the objects we are discussing here. This is the case of Oph-102 (Phan-Bao et al. 2008) and MHO5 (Phan-Bao et al. 2011), among others.

⁴ We recalculated the value of the bolometric luminosity given by Hatchell et al. (2007) to the IC 348 distance adopted in this paper.

Table 4. Summary properties of VeLLOs and FHCs

Source	T_{bol} (K)	L_{bol} (L_{\odot})	L_{int} (L_{\odot})	$M_{\text{env}}^{\text{a}}$ (M_{\odot})	$F_{\text{out}}^{\text{SD b}}$ ($M_{\odot} \text{ km s}^{-1} \text{ yr}^{-1}$)	$F_{\text{out}}^{\text{interf b}}$ ($M_{\odot} \text{ km s}^{-1} \text{ yr}^{-1}$)	Refs. ^c
VeLLOs							
IRAM04191	18	0.15	0.07	0.60	1.5×10^{-5}	–	1
L1521F-IRS	25	0.36	0.04	0.87	–	3.5×10^{-6}	2, 3, 4
L1148-IRS	110	0.12	0.10	0.14	–	1.0×10^{-7}	5
L673-7-IRS	16	0.18	0.04	0.39	1.0×10^{-6}	–	6, 7
L1014-IRS	154	0.15	0.09	0.36	–	5.3×10^{-8}	8, 9
L328-IRS	44	0.14	0.05	0.09	2.0×10^{-7}	–	10, 11
GF9-2	20	0.30	< 0.3	–	6.1×10^{-8}	–	12, 13
J041757B	155	0.003	< 0.003	0.01	–	–	14, 15
IC348-SMM2E	35	0.10	0.06	0.03	–	1.1×10^{-7}	16
FHCs							
Cha-MMS1	20	0.45	0.15	0.80	–	–	17, 18
Per-Bolo58	19	0.18	0.012	1.00	–	5.6×10^{-8}	19, 20
L1448-IRS2E	–	< 0.1	< 0.1	0.50	–	2.5×10^{-5}	21
L1451-mm	30	0.05	< 0.03	0.15	–	8.3×10^{-9}	22
CB17-MMS	< 16	< 0.04	< 0.04	4.0	–	1.3×10^{-7}	23, 24
B1-bS	22	0.31	0.1–0.2	7.3	–	2.4×10^{-6}	25, 26, 27
B1-bN	17	0.15	< 0.03	9.4	–	5.3×10^{-7}	25, 26, 27

^a Envelope masses taken from Kauffmann et al. (2011) when available (being thus the mass measured with a single-dish within a radius of 4200 AU). For objects not included in the compilation of Kauffmann et al. (2011) the envelope masses are those measured with single-dish as reported in the literature.

^b $F_{\text{out}}^{\text{SD}}$ and $F_{\text{out}}^{\text{interf}}$ refer to the outflow force as observed with a single-dish telescope and an interferometer, respectively.

^c Refs: (1) André et al. (1999); (2) Bourke et al. (2006); (3) Takahashi et al. (2013); (4) Onishi, Mizuno & Fukui (1999); (5) Kauffmann et al. (2011); (6) Dunham et al. (2010); (7) Schwarz et al. (2012); (8) Bourke et al. (2005); (9) Maheswar et al. (2011); (10) Lee et al. (2009); (11) Lee et al. (2013); (12) Wiesemeyer et al. (1999); (13) Furuya et al. (2006); (14) Barrado et al. (2009); (15) Palau et al. (2012); (16) this work; (17) Belloche et al. (2006); (18) Tsitali et al. (2013); (19) Enoch et al. (2010); (20) Dunham et al. (2011); (21) Chen et al. (2010); (22) Pineda et al. (2011); (23) Launhardt et al. (2010); (24) Chen et al. (2012); (25) Pezzuto et al. (2012); (26) Huang & Hirano (2013); (27) Hirano & Liu (2014).

2400 AU (Chen et al. 2013; Rodríguez et al. 2014). If this scenario is confirmed, we would be witnessing the formation of a very fragile triple system, of mass ratio ~ 0.1 and widest separation of 2400 AU (corresponding to a binding energy of 9×10^{40} erg). Whether such a fragile system will be disrupted in the future remains an open question, as typical timescales for BD ejection estimated from numerical simulations are around 0.1–0.2 Myr (e.g., Basu & Vorobyov 2012; Bate 2012), comparable to the lifetime of Class 0 objects.

The number of known substellar wide (400–4000 AU) binaries is small (e.g., Luhman et al. 2009; Radigan et al. 2009; Aller et al. 2013; Bonavita et al. 2014), and the SMM2E + SMM2 system constitutes, to the best of our knowledge, the youngest substellar wide multiple system known to date, indicating that the fragmentation process that formed this wide system took place at the earliest stages of star formation. The discovery of the Class 0 proto-BD SMM2E, forming as a scaled-down version of low-mass protostars, and belonging to a wide multiple system, strongly suggests that for this particular case the star formation processes extend down to substellar masses.

6 CONCLUSIONS

We present observations carried out with the SMA of the 870 μm continuum and CO (3–2), ^{13}CO (2–1), and C^{18}O (2–1) emission of IC 348-SMM2E, a faint millimetre source lying near the HH 797 outflow in the IC 348 cluster. We complement these data with archive data from CFHT, *Spitzer*, *Herschel*, and JCMT, and with new CSO observations, allowing us to characterize the main properties of such a faint object. Our main conclusions are summarized as follows:

- We detect two sources at 870 μm , one strong and resolved, called SMM2 and which is the driving source of the HH 797 outflow, and another much fainter, unresolved, and located about 10 arcsec to the (north)east of SMM2, called SMM2E. We estimate a mass of gas and dust of $250 M_{\text{Jup}}$ for SMM2 and $30 M_{\text{Jup}}$ for SMM2E. SMM2E is coincident with recently reported sources at 1.3 mm and 2.1 cm (Chen et al. 2013; Rodríguez et al. 2014).

- The SMA CO (3–2) emission reveals, in addition to the well-known HH 797 outflow, a compact bipolar low-velocity outflow associated with SMM2E. The outflow wings cover 1–2 km s^{-1} , as found in other VeLLOs, and we estimate an outflow mass of $3 \times 10^{-5} M_{\odot}$, a mass outflow rate of $6 \times 10^{-8} M_{\odot} \text{ yr}^{-1}$, and an outflow force of

$10^{-7} M_{\odot} \text{ km s}^{-1} \text{ yr}^{-1}$. An estimate of the mass accretion rate assuming the Shu (1977) model yields $\sim 1.6 \times 10^{-7} M_{\odot} \text{ yr}^{-1}$.

- C^{18}O (2–1) emission is detected towards SMM2E, which shows a velocity gradient perpendicular to the outflow, and corresponds to a dynamical mass of $16 M_{\text{Jup}}$. In addition, the C^{18}O emission allows us to measure the systemic velocities of both SMM2E and SMM2, finding them to be very similar, which suggests SMM2E is gravitationally bound to SMM2 and thus forms a wide (2400 AU) multiple system.

- The analysis of *Spitzer*, *Herschel*, JCMT, and CSO data consistently presents hints of excess of emission at the position of SMM2E. By estimating the fluxes from 70 to 450 μm , and using our collected data and data from the literature, we built the SED for SMM2E, and found that it can be fitted from 70 μm to 2.1 cm with one single modified black-body with a dust temperature of 24 K, a dust emissivity index of 0.8 and a mass envelope of $\sim 35 M_{\text{Jup}}$. Thus, the SED of SMM2E is typical of Class 0 objects.

- The bolometric temperature and luminosity of SMM2E are estimated to be ~ 35 K and $0.10 L_{\odot}$, and the internal luminosity is $\sim 0.06 L_{\odot}$. These properties of SMM2E place the object among the least luminous and most embedded objects known so far, as compared to VeLLOs and FHCs. In addition, SMM2E also presents the smallest envelope mass (measured with single-dish) among the Class 0 VeLLOs and FHCs, strongly suggesting that its final mass will probably remain substellar.

- A comparison of the outflow force for SMM2E to those of other VeLLOs, FHCs, low-mass and intermediate-mass young stellar objects (all measured with an interferometer) shows that SMM2E matches the lower end of the known relation of outflow force vs bolometric luminosity for low-mass protostars, suggesting that in this case the formation of this proto-BD candidate can be explained as a scaled-down version of low-mass stars.

ACKNOWLEDGEMENTS

We are deeply grateful to Helen Kirk, Josh Walawender, and Dough Johnstone for sharing the 450 μm JCMT data, and to Jackie Davidson, and Giles Novak for sharing 350 μm CSO data to compare to the new data acquired at the CSO. The authors are also grateful to the referee for her/his comments that significantly improved the paper. A.P., L.A.Z., and L.F.R. acknowledge the financial support from UNAM, and CONACyT, México. H.B. is funded by the Spanish Ramón y Cajal fellowship program number RYC-2009-04497. This research has been funded by Spanish grants AYA2010-21161-C02-02, and AYA2012-38897-C02-01. D. Li acknowledges the support from National Basic Research Program of China (973 program) No. 2012CB821800 and NSFC No. 11373038. This research used the facilities of the Canadian Astronomy Data Centre operated by the National Research Council of Canada with the support of the Canadian Space Agency. Based on observations obtained with MegaPrime/MegaCam, a joint project of CFHT and CEA/DAPNIA, at the Canada-France-Hawaii Telescope (CFHT) which is operated by the National Research Council (NRC) of Canada, the Institut National des Sciences de l'Univers of the Centre National de la Recherche

Scientifique of France, and the University of Hawaii. Based on observations obtained with WIRCam, a joint project of CFHT, Taiwan, Korea, Canada, France, and the Canada-France-Hawaii Telescope (CFHT) which is operated by the National Research Council (NRC) of Canada, the Institut National des Sciences de l'Univers of the Centre National de la Recherche Scientifique of France, and the University of Hawaii. This work is based in part on data obtained as part of the UKIRT Infrared Deep Sky Survey, made use of VOSA, developed under the Spanish Virtual Observatory project supported from the Spanish MICINN through grant AyA2008-02156, and of the SIMBAD database, operated at CDS, Strasbourg, as well as Topcat (Taylor 2005).

REFERENCES

- Aller K. M., et al., 2013, *ApJ*, 773, 63
 André P., Ward-Thompson D., Barsony M., 1993, *ApJ*, 406, 122
 André P., Motte F., Bacmann A., 1999, *ApJ*, 513, L57
 André P. et al., 2010, *A&A*, 518, L102
 André P., Di Francesco J., Ward-Thompson D., Inutsuka S.-i., Pudritz R. E., Pineda J., 2013, arXiv, arXiv:1312.6232
 Baraffe I., Chabrier G., Allard F., Hauschildt P. H., 2002, *A&A*, 382, 563
 Barrado D., et al., 2009, *A&A*, 508, 859
 Basu S., Vorobyov E. I., 2012, *ApJ*, 750, 30
 Bate M. R., 2012, *MNRAS*, 419, 3115
 Bate M. R., Bonnell I. A., Bromm V., 2002, *MNRAS*, 332, L65
 Bate M. R., Tricco T. S., Price D. J., 2014, *MNRAS*, 437, 77
 Belloche A., Parise B., van der Tak F. F. S., Schilke P., Leurini S., Güsten R., Nyman L.-Å., 2006, *A&A*, 454, L51
 Beltrán, M. T., Estalella, R., Anglada, G., Rodríguez, L. F., Torrelles, J. M. 2001, *AJ*, 121, 1556
 Beltrán M. T., Estalella R., Girart J. M., Ho P. T. P., Anglada G., 2008, *A&A*, 481, 93
 Bertin E., 2006, *ASPC*, 351, 112
 Bertin E., Mellier Y., Radovich M., Missonnier G., Didelon P., Morin B., 2002, *ASPC*, 281, 228
 Bonavita M., Daemgen S., Desidera S., Jayawardhana R., Janson M., Lafreniere D., 2014, arXiv:1406.7298
 Bontemps, S., André, P., et al. 1996, *A&A*, 311, 858
 Boss A. P., Yorke H. W., 1995, *ApJ*, 439, L55
 Bourke, T. L., et al. 2005, *ApJ*, 633, L129
 Bourke T. L., et al., 2006, *ApJ*, 649, L37
 Briggs, D. 1995, PhD Thesis, New Mexico Inst. of Mining and Technology
 Busquet G., et al., 2013, *ApJ*, 764, L26
 Chabrier G., Johansen A., Janson M., Rafikov R., 2014, arXiv, arXiv:1401.7559
 Chapman N. L., et al., 2013, *ApJ*, 770, 151
 Chen, H., Myers, P. C., Ladd, E. F., Wood, D. O. S. 1995, *ApJ*, 445, 377
 Chen X., Arce H. G., Zhang Q., Bourke T. L., Launhardt R., Schmalzl M., Henning T., 2010, *ApJ*, 715, 1344
 Chen X., Arce H. G., Dunham M. M., Zhang Q., Bourke T. L., Launhardt R., Schmalzl M., Henning T., 2012, *ApJ*, 751, 89
 Chen X., et al., 2013, *ApJ*, 768, 110
 Chin Y.-N., Henkel C., Whiteoak J. B., Langer N., Churchwell E. B., 1995, *VizieR Online Data Catalog*, 330, 50960
 di Francesco J., Evans N. J., II, Caselli P., Myers P. C., Shirley Y., Aikawa Y., Tafalla M., 2007, in Reipurth B., Jewitt D., Keil K., eds., *Protostars & Planets V*. Univ. Arizona Press, Tucson, p. 17
 Davidson J. A., et al., 2011, *ApJ*, 732, 97
 Dowell C. D., et al., 2003, *SPIE*, 4855, 73

- Duarte-Cabral A., Bontemps S., Motte F., Hennemann M., Schneider N., André P., 2013, *A&A*, 558, A125
- Dunham M. M., Vorobyov E. I., 2012, *ApJ*, 747, 52
- Dunham M. M., Crapsi A., Evans N. J., II, Bourke T. L., Huard T. L., Myers P. C., Kauffmann J., 2008, *ApJS*, 179, 249
- Dunham, M. M., Evans, N. J., Bourke, T. L., et al. 2010, *ApJ*, 721, 995
- Dunham M. M., Chen X., Arce H. G., Bourke T. L., Schnee S., Enoch M. L., 2011, *ApJ*, 742, 1
- Enoch, M. L., Evans II, N. J., Sargent, A. I., & Glenn, J. 2009, *ApJ*, 692, 973
- Enoch M. L., Lee J.-E., Harvey P., Dunham M. M., Schnee S., 2010, *ApJ*, 722, L33
- Evans N. J., II, et al., 2009, *ApJS*, 181, 321
- Fernández-López M., Girart J. M., Curiel S., Zapata L. A., Fonfría J. P., Qiu K., 2013, *ApJ*, 778, 72
- Frerking, Langer, Wilson 1982, *ApJ*, 262, 590
- Froebrich D., Schmeja S., Smith M. D., Klessen R. S., 2006, *MNRAS*, 368, 435
- Furuya R. S., Kitamura Y., Shinnaga H., 2006, *ApJ*, 653, 1369
- Goldsmith P. F., Heyer M., Narayanan G., Snell R., Li D., Brunt C., 2008, *ApJ*, 680, 428
- Gooch, R. 1996, in *ASP Conf. Ser. 101, Astronomical Data Analysis Software and Systems V*, ed. G. H. Jacoby & J. Barnes (San Francisco, CA: ASP), 80
- Hacar A., Tafalla M., Kauffmann J., Kovács A., 2013, *A&A*, 554, A55
- Hara C., et al., 2013, *ApJ*, 771, 128
- Hartmann, L. 1998, in *Accretion Processes in Star Formation*, ed. A. King et al. (New York: Cambridge Univ. Press), 92
- Hatchell J., Fuller G. A., Richer J. S., Harries T. J., Ladd E. F., 2007, *A&A*, 468, 1009
- Hennebelle P., Chabrier G., 2008, *ApJ*, 684, 395
- Hester J. J., et al., 1996, *AJ*, 111, 2349
- Hirano N., Liu, F.-C., 2014, *ApJ*, 789, 50
- Hirota T., Honma M., Imai H., Sunada K., Ueno Y., Kobayashi H., Kawaguchi N., 2011, *PASJ*, 63, 1
- Hirota T., et al., 2008, *PASJ*, 60, 37
- Ho P. T. P., Moran J. M., Lo K. Y., 2004, *ApJ*, 616, L1
- Hsieh T.-H., Lai S.-P., 2013, *ApJS*, 205, 5
- Huang Y.-H., Hirano N., 2013, *ApJ*, 766, 131
- Jørgensen, J. K., Harvey, P. M., Evans, N. J., II, et al. 2006, *ApJ*, 645, 1246
- Kauffmann, J., Bertoldi, F., Bourke, T. L., et al. 2011, *MNRAS*, 416, 2341
- Larson, R. B. 1969, *MNRAS*, 145, 271
- Launhardt R., et al., 2010, *ApJS*, 188, 139
- Lee C. W., et al. 2009, *ApJ*, 693, 1290
- Lee C. W., Kim M.-R., Kim G., Saito M., Myers P. C., Kurono Y., 2013, *ApJ*, 777, 50
- Li H., Dowell C. D., Kirby L., Novak G., Vaillancourt J. E., 2008, *ApOpt*, 47, 422
- Luhman K. L., Mamajek E. E., Allen P. R., Muench A. A., Finkbeiner D. P., 2009, *ApJ*, 691, 1265
- Machida M. N., Inutsuka S.-i., Matsumoto T., 2008, *ApJ*, 676, 1088
- Maheswar G., Lee C. W., Dib S., 2011, *A&A*, 536, A99
- Murillo N. M., Lai S.-P., 2013, *ApJ*, 764, L15
- Myers P. C., 2014, *ApJ*, 781, 33
- Myers P. C., Adams F. C., Chen H., & Schaff E. 1998, *ApJ*, 492, 703
- Offner S. S. R., Lee E. J., Goodman A. A., Arce H., 2011, *ApJ*, 743, 91
- Omukai K., 2007, *PASJ*, 59, 589
- Onishi T., Mizuno A., Fukui Y., 1999, *PASJ*, 51, 257
- Ossenkopf, V. & Henning, T. 1994, *A&A*, 291, 943
- Ott S., 2010, *ASPC*, 434, 139
- Padoan, P., & Nordlund, Å. 2004, *ApJ*, 617, 559
- Palau A., et al., 2006, *ApJ*, 636, L137
- Palau A., Estalella R., Ho P. T. P., Beuther H., Beltrán M. T., 2007, *A&A*, 474, 911
- Palau A., et al., 2012, *MNRAS*, 424, 2778
- Palau A., Sánchez Contreras C., Sahai R., Sánchez-Monge Á., Rizzo J. R., 2013, *MNRAS*, 428, 1537
- Palmeirim P., et al., 2013, *A&A*, 550, A38
- Pech G., Zapata L. A., Loinard L., Rodríguez L. F., 2012, *ApJ*, 751, 78
- Pety J., Gueth F., Guilloteau S., Dutrey A., 2006, *A&A*, 458, 841
- Pezzuto S., et al., 2012, *A&A*, 547, A54
- Phan-Bao, N., Riaz, B., Lee, C.-F., et al. 2008, *ApJ*, 689, L141
- Phan-Bao N., Lee C.-F., Ho P. T. P., Tang Y.-W., 2011, *ApJ*, 735, 14
- Phan-Bao N., Lee C.-F., Ho P. T. P., Martin E. L., 2014, *A&A*, in press, arXiv:1403.1926
- Pineda J. E., et al., 2011, *ApJ*, 743, 201
- Poglitsch A., et al., 2010, *A&A*, 518, L2
- Radigan J., Lafrenière D., Jayawardhana R., Doyon R., 2009, *ApJ*, 698, 405
- Rebull L. M., et al., 2007, *ApJS*, 171, 447
- Reipurth, B., & Clarke, C. 2001, *AJ*, 122, 432
- Rice, W. K. M., Armitage, P. J., Bonnell, I. A., et al. 2003, *MNRAS*, 346, L36
- Rodríguez L. F., Zapata L. A., Palau A. 2014, *ApJ*, 790, 80
- Roussel H., 2013, *PASP*, 125, 1126
- Sadavoy S. I., et al., 2014, *ApJ*, 787, L18
- Saigo K., Tomisaka K., 2006, *ApJ*, 645, 381
- Sault, R. J., Teuben, P. J., & Wright, M. C. H. 1995, *Astronomical Data Analysis Software and Systems IV*, 77, 433
- Schwarz K. R., Shirley Y. L., Dunham M. M., 2012, *AJ*, 144, 115
- Scoville N. Z., Carlstrom J. E., Chandler C. J., Phillips J. A., Scott S. L., Tilanus R. P. J., Wang Z., 1993, *PASP*, 105, 1482
- Shu F. H., 1977, *ApJ*, 214, 488
- Sorahana S., Yamamura I., Murakami H., 2013, *ApJ*, 767, 77
- Stassun K. G., Kratter K. M., Scholz A., Dupuy T. J., 2012, *ApJ*, 756, 47
- Takahashi S., Ho P. T. P., 2012, *ApJ*, 745, L10
- Takahashi S., Ohashi N., Bourke T. L., 2013, *ApJ*, 774, 20
- Taylor M. B., 2005, *ASPC*, 347, 29
- Terebey S., Van Buren D., Brundage M., Hancock T., 2006, *ApJ*, 637, 811
- Tsitali A. E., Belloche A., Commerçon B., Menten K. M., 2013, *A&A*, 557, A98
- Umbreit S., Burkert A., Henning T., Mikkola S., Spurzem R., 2005, *ApJ*, 623, 940
- Walawender J., Bally J., Kirk H., Johnstone D., Reipurth B., Aspin C., 2006, *AJ*, 132, 467
- Whitworth A. P., Zinnecker H., 2004, *A&A*, 427, 299
- Wiesemeyer H., Cox P., Gusten R., Zylka R., 1999, *ESASP*, 427, 533
- Wu, Y., Wei, Y., et al. 2004, *A&A*, 426, 503
- Young C. H., et al. 2004, *ApJS*, 154, 396
- Young C. H., & Evans N. J., II 2005, *ApJ*, 627, 293

APPENDIX A: CO (3–2) AND C¹⁸O (2–1) CHANNEL MAPS

In Figs. A1 and A2 we present the channel maps of the CO (3–2) and C¹⁸O (2–1) emission as observed with the SMA, and centred on SMM2E. The emission associated with SMM2 is part of the HH 797 large-scale outflow (Pech et al., in prep.).

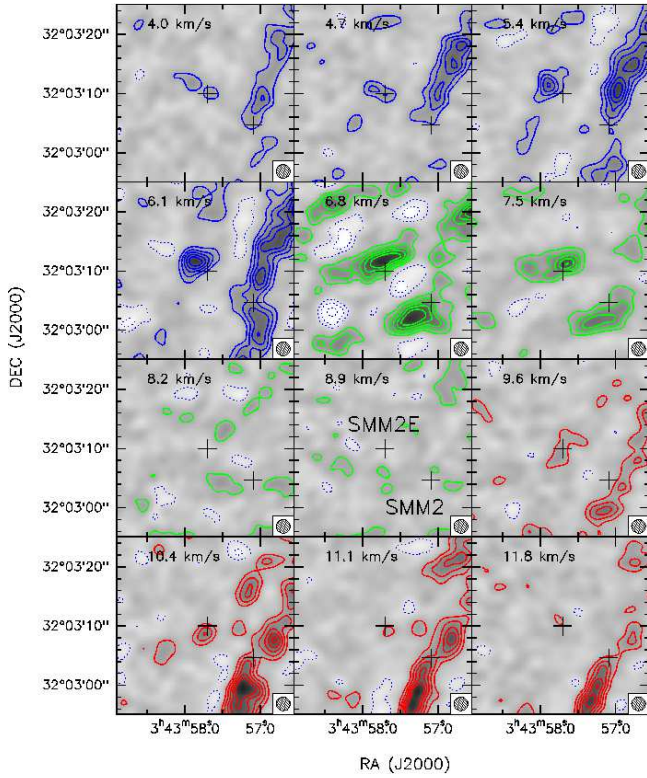


Figure A1. SMA CO (3–2) channel maps centred on SMM2E. The plus signs correspond to SMM2E (left) and SMM2 (right). Contours are $-6, -4, -2, 2, 4, 6, 8,$ and 10 times $0.85 \text{ Jy beam}^{-1}$. The velocity of each channel is indicated in the top-left corner, and the beam is shown in the bottom-right corner of each panel.

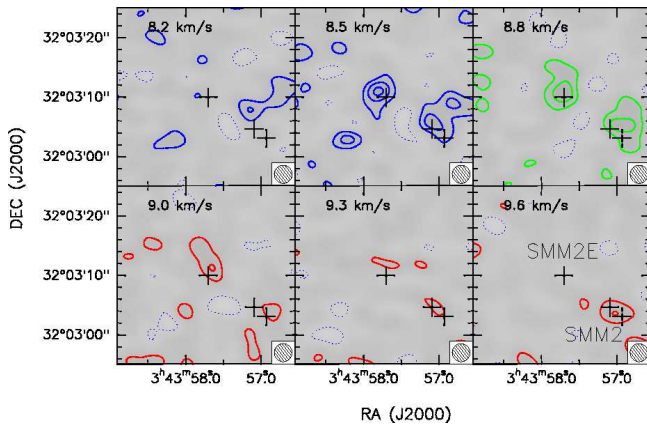


Figure A2. SMA C^{18}O (2–1) channel maps centred on SMM2E. The plus signs correspond to SMM2E (left), SMM2-JVLA3b (centre), and SMM2-JVLA3a (right, Rodríguez et al. 2014). Contours are $-6, -4, -2, 2, 4,$ and 6 times $0.25 \text{ Jy beam}^{-1}$. The velocity of each channel is indicated in the top-left corner, and the beam is shown in the bottom-right corner of each panel.